Check for updates

Uncovering the Origin of Chirality from Plasmonic Nanoparticle/Cellulose Nanocrystal Composite Films

Sixiang Zhao, Han Zhu, Jicun Lu, Ming Li, Liancheng Zhao, Lei Zhou,* and Liming Gao*

Chirality generated by the co-assembly of plasmonic nanoparticles (NPs) and chiral photonic crystals has attracted broad interest owing to its strong optical activities. However, it is difficult to understand the physical mechanism of the unique chiral responses, for surface-plasmon-mediated circular dichroism (SP-CD) is a hybrid response generated from chiral plasmonic–photonic systems. This study aims to investigate how chirality is generated by this system and the relationship between SP-CD and plasmonic–photonic couplings. Here, quasi-continuous plasmon bands are designed to interact with the different photonic bandgaps of cellulose nanocrystals (CNCs). In spectroscopy and simulation, characteristic SP-CD shape lines derived from the extinction dispersion of plasmonic NPs for circularly polarized light in the CNCs are observed. It is demonstrated that this plasmonic chirality is determined by the coupling states and originates from a multiple scattering combination of plasmonic NPs under a chiral excitation field. A novel transfer-matrix method is established to perform numerical analysis of this complex multiple scattering efficiently. This study is expected to offer a deep insight into chiral plasmonic–photonic systems.

1. Introduction

Chirality, a widely existing phenomenon in nature, from small molecules to macrocosms, is used to describe any object that cannot be superimposed on its mirror image.[1] Chirality can be observed not only in geometrical structures but also in optics. Non-identical absorption of right- and left-handed circularly polarized (RCP and LCP) light, called circular dichroism (CD),

is observed when light passes through a chiral object.[2] The CD of plasmonic chirality differs from that of natural chiral molecules, for the different RCP and LCP light absorption of plasmonic systems caused by the collective electron oscillations of metal nanoparticles (NPs).[3–5] The mechanisms of generating plasmonic chirality in previous studies can be classified into two types: molecular-induced plasmonic chirality and structural plasmonic chirality. The molecular-induced plasmonic chirality is derived from the Coulomb interaction that occurs when chiral molecules are attached to the surface plasmonic materials.[6–9] Structural plasmon chirality involves the construction of chiral arrangements of plasmon materials by assembly or lithography.[10–13] The novel plasmonic chirality opens up potential applications, such as chemical and biological sensing,[14,15] negative-refraction metamaterials,[16] circularly polarized light detection,[17] and nonlinear optics.[18] Further study of plasmonic chirality is expected to lead to advanced interactions with light, leading to more optics and photoelectric device applications.

As bottom-up methods for synthesizing chiral plasmonic materials, assembling metallic nanostructures with chiral templates, such as supramolecular assembly, DNA origami, peptide organization, and cholesteric liquid crystals, are exceptionally promising approaches for designing chiral plasmonic materials.[8,19–21] Using the above methods, surface-plasmon-mediated CD (SP-CD) signals are generated from the plasmons along with a helical structure. In some situations, these SP-CD signals are ensemble chiral responses derived from chiral plasmons and chiral templates. Therefore, understanding CD signals from plasmonic chirality in chiral matrices is much more difficult than independent plasmon CD signals from metallic chiral structures.

Cellulose nanocrystals (CNCs) with the intrinsic characteristics of cholesteric liquid crystals and photonic crystals, can be easily extracted from natural cellulose fibrils via acid hydrolysis.[22,23] CNCs are easy to disperse in aqueous solutions with extreme stability, because they are functionalized by sulfate ester groups and have the electrostatic repulsion of CNCs in aqueous solution.[24,25] Surprisingly, CNCs can spontaneously self-assemble into a chiral cholesteric liquid crystalline phase with a left-handed chiral helical structure derived from entropic steric interactions, referred to as the evaporation-induced assembly (EISA) process.[26,27] This cholesteric structure

S. Zhao, M. Li, L. Zhao, L. Gao
State Key Laboratory of Metal Matrix Composites
School of Materials Science and Engineering
Shanghai Jiao Tong University
Shanghai 200240, P. R. China
E-mail: liming.gao@sjtu.edu.cn

H. Zhu, L. Zhou
State Key Laboratory of Surface Physics
Key Laboratory of Micro and Nano Photonic Structures
(Ministry of Education) and Department of Physics
Fudan University
Shanghai 200438, P. R. China
E-mail: phzhou@fudan.edu.cn

J. Lu
Academy for Engineering & Technology
Fudan University
Shanghai 200433, P. R. China

The ORCID identification number(s) for the author(s) of this article can be found under https://doi.org/10.1002/adfm.202201927.

imparts the selective reflection of LCP light and transmission of RCP light with a photonic bandgap (PBG). Furthermore, the PBG of CNC films can be tuned over a large range using different methods, such as ultrasonication (redshift), or adding an electrolyte (blueshift).[28] When guest NPs are added to CNCs during an EISA process, excluded-volume effects prompt the NPs to orient along the CNCs. The orientations of guest NPs among the CNCs influence the accessible volume of the CNCs. When the concentration increases during drying, the CNCs tend to compel NPs to orient along the CNCs for larger excluded volumes.[29] Therefore, CNCs are well-suited as chiral templates for the fabrication of chiral composite films.[30]

In the case of plasmonic chirality, various plasmonic NPs were incorporated into the CNC films to produce plasmonic chirality, and a specific CD line shape was observed. Significant dips were repeatedly observed in the CD spectra of AuNP/CNC composite films.[31,32] However, the mechanism of forming these specific CD line shapes and the intrinsic relationship between the CD line shapes and plasmonic–photonic systems remains unclear.

In this study, we systematically investigated how the characteristic SP-CD signals generated by the interaction between quasi-continuous plasmon bands and different PBGs in such systems. We noticed that the formation and shifts of the characteristic SP-CD are highly related to the states of plasmonic–photonic coupling. By simulating plasmonic–photonic couplings, extinction dispersions of plasmons for LCP and RCP light in PBGs were observed, demonstrating the origin of characteristic SP-CD signals and plasmonic CD. The extinction dispersions for circularly polarized light were further proven to be generated by a multiple scattering combination of plasmonic NPs in a chiral excitation field. In addition, we established a novel transfer-matrix method to efficiently perform numerical analyses of this complex multiple scattering.

2. Results and Discussion

In this study, CNCs were extracted from microcrystalline cellulose (MCC), produced by partly depolymerization of natural cellulose. Commercial MCC was hydrolyzed using 64 wt% sulfuric acid to remove amorphous components and a spindle-like morphology of the CNC nanorods was obtained. The transmission electron microscopy (TEM) image is shown in Figure S1a (Supporting Information). The length of the spindle-like CNCs is ≈170 nm, and their size distribution was measured using dynamic light scattering (DLS) (Figure S1b, Supporting Information). The electrokinetic potential (ζ-potential) of the CNCs, which was derived from the negatively charged sulfate ester groups, was −46 mV. An adequate ζ-potential is the basis for both the colloidal stability of CNC suspensions and their ability to self-assemble into cholesteric liquid crystals.

Three types of CNC templates with different PBGs were fabricated to investigate different plasmonic–photonic couplings using 4 mL of 1.5 wt% CNC suspension, 4 mL of 3.5 wt % CNC suspension, and 4 mL of 3.5 wt % CNC suspension with extra NaCl (50 µL of 0.1 M NaCl) denoted as CNC-1, CNC-2, and CNC-3, respectively. Figure S2a–c (Supporting Information) shows cross-sectional scanning electron microscopy (SEM)

images of the CNC films, which illustrate the periodic structures of cholesteric CNC films. The space between the layers that rotate along the helical axis after 360° is typically defined as the pitch of the films. At certain wavelengths, the films strongly reflect LCP light and efficiently transmit RCP light. Selectively reflection bands also referred to as PBGs are related to pitches according to the following equation:

$$\lambda_{PB} = nP\sin\theta \tag{1}$$

where n is the effective refractive of CNC films, P is the pitch of helix structure, and θ is the angle between the incident light and the CNC layers. 50 µL of 0.1 M NaCl was added to the CNC suspension to decrease the pitch of the CNC films and obtain a blue shift of the PBG because the surface charge of CNCs was weakened by the electrolyte. Figure S3a (Supporting Information) shows the variation in PBGs in the UV–Vis–NIR transmission spectra of the CNC films. After adding 50 µL of 0.1 M NaCl, an obvious blue shift of the PBG appeared with a decrease in the CNC pitches. In addition, a small blue shift in the PBG of the 1.5 wt% CNC film was observed when compared with the 3.5 wt% CNC film, owing to a decrease in the initial concentration.[28] The CD spectra shown in Figure S3b (Supporting Information) illustrates a similar trend to the transmission spectra because the main extinction of light is attributed to the selective reflection of LCP light. CD is defined as the difference in the extinction of LCP and RCP light and is expressed as,

$$CD = Ext_{LCP} - Ext_{RCP} \tag{2}$$

where Ext_{LCP} and Ext_{RCP} are the extinction of LCP and RCP light, respectively.

To generate different states of plasmonic–photonic couplings, quasi-continuous plasmon bands were obtained by precisely controlling the morphologies of gold bipyramid-based nanoparticles (AuBNPs). **Figure 1**a shows the morphology control process and the TEM images of a series of AuBNPs. Initially, the original gold bipyramids were synthesized using a seed-mediated growth method for further modification. The original gold bipyramids were then regrown into three types of AuBNPs (bipyramid-like NPs, dumbbell-like NPs, and bifrustum-like NPs) using the singular surfactant method, binary surfactant method, and regrowth after etching. Furthermore, the concentrations of Ag⁺ and pH of the regrowth solutions were adjusted to achieve fine adjustments of the plasmon bands of AuBNPs in the singular and binary surfactant method. The regrowth after etching process was conducted to produce larger blue shifts of plasmon bands.

For the singular surfactant method, only hexadecyl trimethyl ammonium bromide (CTAB) was used as a capping agent to synthesize bipyramid-like NPs. The regrowth with CTAB resulted in a similar morphology to the original bipyramids but with varying aspect ratios owing to the differential growth rates in different directions controlled by the solution pH and concentrations of Ag⁺. The bipyramid-like NPs that were regrown with a singular surfactant (CTAB) are denoted as S-1 and S-2. For the binary surfactant method, mixed surfactants (Hexadecyltrimethylammonium chloride (CTAC):CTAB = 90:1) were applied to increase the growth rates on the tips of the AuBNPs
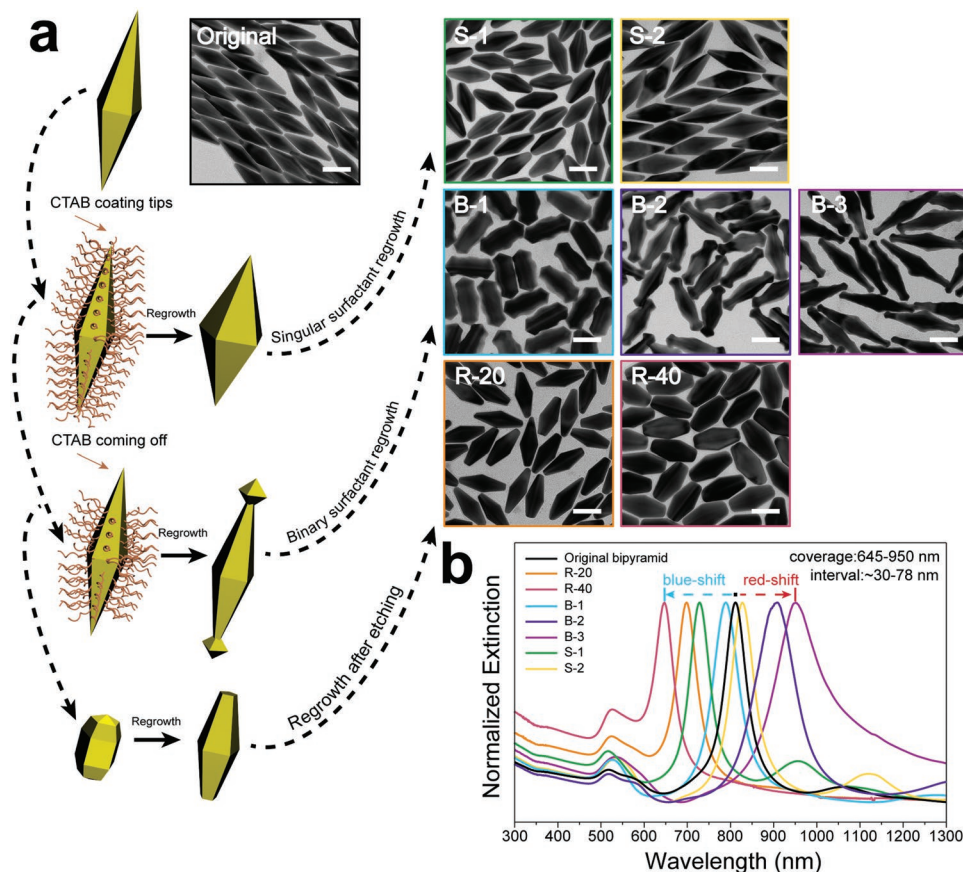
Figure 1. Characterization of AuBNPs. a) Schematic of the fabrication process of AuBNPs and TEM images of a series of AuBNPs. Scale bar: 50 nm. b) UV–Vis–NIR extinction spectra of a series of AuBNPs.

and synthesize dumbbell-like NPs. When mixed surfactants are used in the regrowth of bipyramids, CTAC binds more easily to the tip region of the bipyramids than CTAB, and the weaker binding affinities of CTAC result in additional growth on the tips. This extra growth on the tips brings about a fine-tuning of the plasmon bands of AuBNPs and can be used to extend tuning ranges in combination with adjustments of the solution pH and concentrations of Ag^+. The dumbbell-like NPs (denoted as B-1, B-2, and B-3) were synthesized using regrowth solution with varying solution pHs and of Ag^+.

In the presence of CTAB or mixed surfactants, the amounts of Ag^+ and pH were closely associated with the growth rates of AuBNPs. Ag^+ ions can block certain facets by underpotential deposition to slow down the growth rate. Increasing the pH of the growth solution promoted growth rates in all directions of the bipyramids leading to low aspect ratios. The roles of Ag^+ ions and pH are discussed in more detail in Supporting Information. AuBNPs were etched to form smaller NPs for regrowth with an $HAuCl_4$ solution, which acted as an etching agent by oxidizing Au^0 atoms to Au^+. After the AuBNPs were etched for 20 or 40 min, the etched NPs underwent regrowth to form bifrustum-like NPs (denoted R-20 and R-40, respectively). The regrowth of the etched bipyramids gives the plasmon peaks of AuBNPs large blue shifts compared to the original gold bipyramids. The UV–Vis–NIR extinction spectra of a series of AuBNPs are shown in Figure 1b, which exhibit a wide range

(645–950 nm) and narrow peak intervals (≈30–78 nm) of longitudinal surface plasmon resonance (LSPR) obtained by precise morphological adjustments.

Figure 2a shows the process of evaporation-induced co-assembly and chiral composite structures formed after co-assembly. After the co-assembly, the composite films still formed a uniform layered structure of left-handed cholesteric CNC, as shown in Figure 2b. In addition, the arrangement of AuBNPs followed the cholesteric structure of the CNC template, as shown in the cross-sectional TEM image (Figure 2b). Figure 2c shows the interaction of the chiral composite films with circularly polarized light. When circularly polarized light propagates through the chiral composite films, it interacts with not only the cholesteric structure of CNCs but also the helical distribution of AuBNPs. In previous studies, different metallic nanostructures were incorporated into CNC films, and the CD spectra of these chiral composite films were measured to investigate the interaction between circularly polarized light and CNC/metallic nanostructure chiral films. Noticeable dips in the CD spectra were observed in most cases and were considered "plasmonic dips", which are associated with metallic nanostructures.[31,32]

However, it is difficult to determine whether the plasmonic dips are caused by the overlap of independent CD signals from cholesteric CNCs and the chiral distribution of NPs or modification by the achiral extinction of NPs on CNC CD signals.
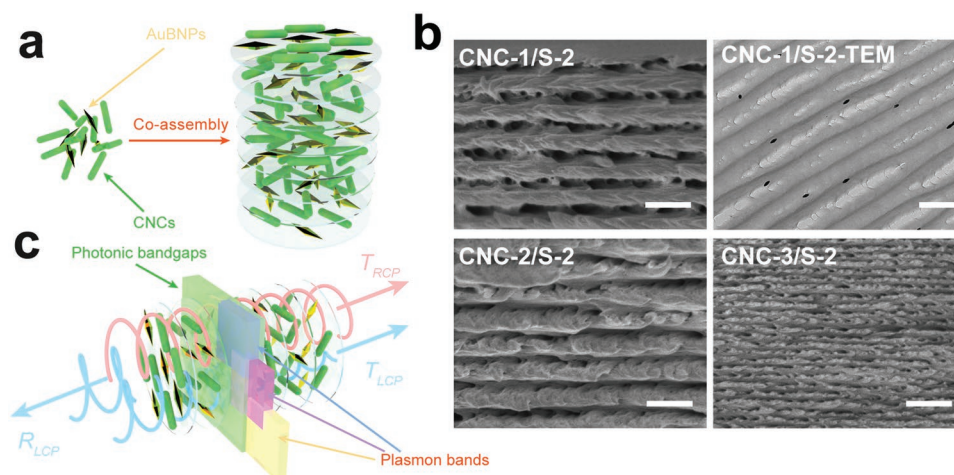
Figure 2. a) Schematic of the evaporation-induced co-assembly process. b) Cross-sectional SEM images of AuBNP (S-2) incorporated with CNC-1, CNC-2, and CNC-3 films, and cross-sectional TEM image of the CNC-1/S-2 chiral composite film. Scale bar: 500 nm. c) Schematic of the interaction between circularly polarized light and chiral composite films.

The explanation of this problem directly relates to whether the plasmonic chirality of NPs in CNCs exists. Therefore, it is necessary to carefully analyze the components of CD signals and study how the states of plasmonic–photonic couplings influence CD signals. To answer the abovementioned questions, the different CNC templates and AuBNPs were used to fabricate chiral composite films for further spectroscopy analysis.

The CD spectra of 1.5 wt% CNCs (CNC-1) assembled with a series of AuBNPs are shown in **Figure 3**. It should be pointed out that the LSPR peaks of the composite films are redshifted compared to the LSPR peaks of AuBNP dispersions, which is associated with the increase in the medium refractive index from water to CNCs.[33] In Figure 3b, the relative positions between the LSPR peaks and the PBG display the degrees of plasmonic–photonic couplings according to the UV–Vis–NIR transmission spectra (Figure S14, Supporting Information) of the chiral composite films. In Figure 3a,c, the plasmonic–photonic coupling effect observably modified the line shapes in the CD spectra. For R-20 and R-40, when plasmon bands were coupled with the left side of the PBG, the characteristic dip-peak line shapes of the CD spectra were observed. For S-1, 2, and B-1, when plasmon bands were coupled with the right side of the PBG, the peak-dip-peak line shapes of the CD curves were produced. The continuous shifts of the dips and peaks, along with the shifts of the plasmonic–photonic coupling position, indicate that the coupling effect leads to the characteristic CD line shapes. It is considered that the relatively small second peak of S-2 CD is caused by the weak coupling between the plasmon band of S-2 and the edge of the PBG because the CD spectra return to a normal shape with the uncoupling between the plasmonic bands of B-2, 3 and the PBG.

To investigate the characteristic CD line shapes caused by plasmonic–photonic couplings, CD spectra were produced by simulating the left-handed helical distribution of AuBNPs in a CNC refractive index background with the same helical orientation. In Figure 3d, the dip-peak and peak-dip-peak shapes of the simulated CD curves are highly consistent with the experimental measurements, indicating that the simulations success-

fully reproduced unique CD responses. Using the simulation results, the LCP and RCP light extinction of the AuBNPs can be separated from the background CNC CD signals. The extinction spectra of the AuBNPs for LCP and RCP light are shown in Figure 3e. An obvious dispersion of the extinction wavelengths for the LCP and RCP light can be observed. The extent of extinction dispersion is determined by the degree of the plasmonic–photonic couplings, for the extent of extinction dispersion decrease with coupling position from the center to the edge of the PBG. The extinction dispersion for LCP and RCP light can be used to explain the formation of the characteristic dip-peak and peak-dip-peak line shapes. First, the peak-dip-peak shape can be considered a dip-peak with a left-side CNC CD peak when the plasmon bands couple with the PBG on the right side. The ensemble CD was decreased by the extinction of RCP light from AuBNPs at shorter wavelengths and was increased by the extinction of LCP light at longer wavelengths, which resulted in dip-peak and peak-dip-peak line shapes, when the extinction dispersion of AuBNPs occurred on the left side and right side of the PBG, respectively. In addition, the extinction dispersion for LCP and RCP light forms independent CD signals of AuBNPs, which can be considered evidence of plasmonic chirality (Figure 3i). Notably, when the plasmon bands and PBG uncouple, the differences in extinction wavelengths disappear. The disappearance induced the CD signals of the chiral composite films to return to the normal line shape. Within the PBG of CNCs, the left-handed chiral structure of CNCs provide ongoing reflections of LCP light, which generates the nonuniform background for different location of AuBNPs in chiral distribution and the asymmetry excitation fields with respect to LCP and RCP. It provides the AuBNPs in chiral distributions with different LCP and RCP excitations and scatterings, which generate the different intensity of local electric field under LCP and RCP light (Figure 3g,h) and the different oscillation of surface plasmons (Figure 3f). Therefore, the chiral excitation field generated by CNCs plays an important role in the chiral response of AuBNPs. The extinction dispersions and independent CD of AuBNPs can be regarded as interference results of a multiple scattering combination of
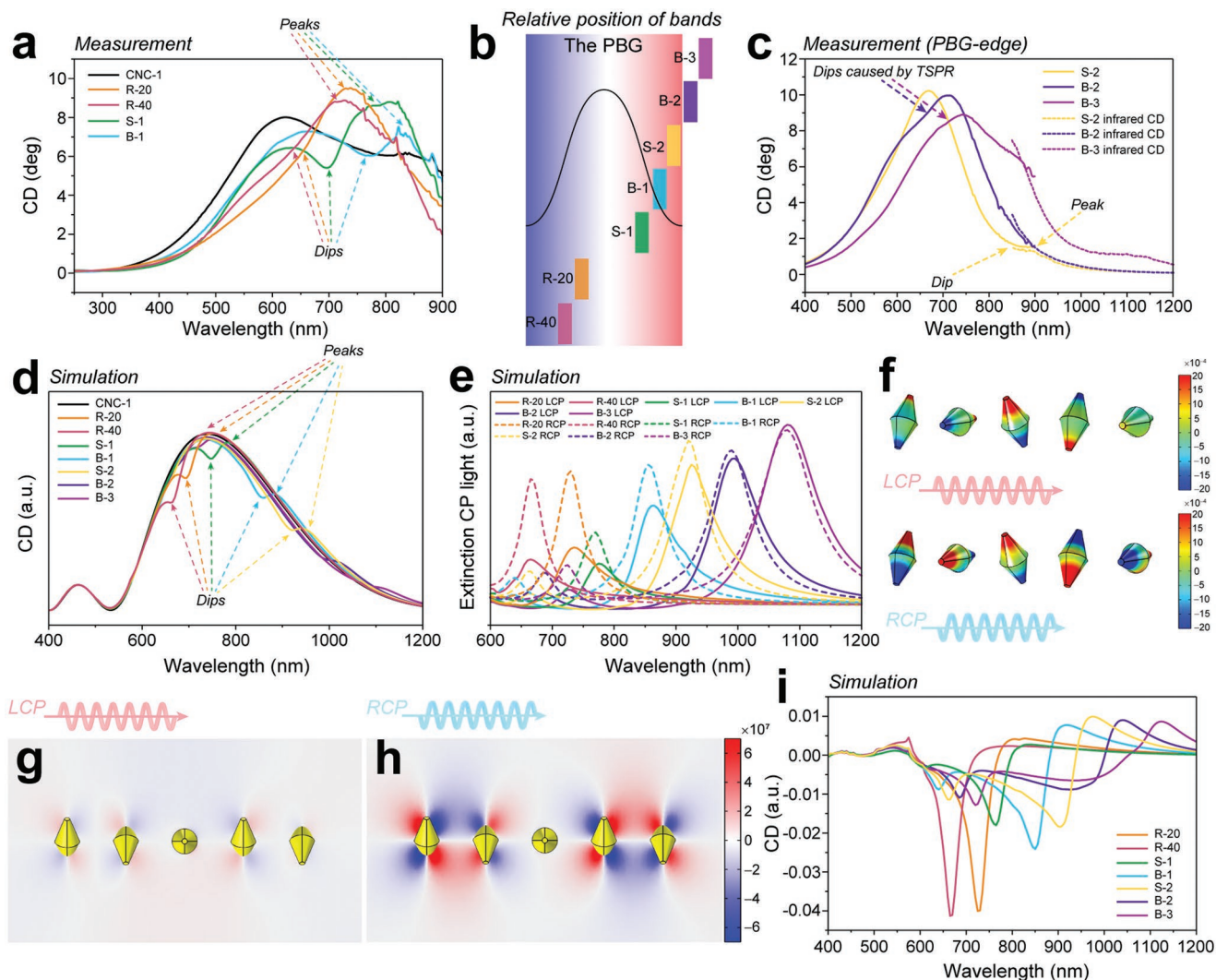
Figure 3. a) Measured CD spectra of AuBNP (R-20, R-40, S-1, and B-1)/CNC-1 composite films and the CNC-1 film. b) Schematic of relative positions between plasmon bands and the PBG of CNC-1. c) Measured CD spectra of AuBNP (S-2, B-2, and B-3)/CNC-1 composite films. d) Simulated CD spectra of AuBNP/CNC composite films and the CNC film. e) Simulated extinction spectra for LCP and RCP light of AuBNPs in CNC background. f) LCP and RCP light induced surface charge distribution profiles of AuBNPs in CNC background. g) LCP light induced local electric field of AuBNP/CNC. h) RCP light induced local electric field of AuBNP/CNC. i) Simulated independent CD spectra of AuBNPs with plasmonic–photonic coupling states.

plasmonic NPs under a chiral excitation field. In addition, when the transverse surface plasmon resonance (TSPR) of AuBNPs has sufficient intensity, it can generate similar plasmonic–photonic couplings to LSPR and produce dip-peak line shapes (Figure 3c). The defects in chiral composite films and model simplification of AuBNPs in simulation can bring slight mismatching between measurements and simulations. The changes in CD responses caused by defects in CNCs and changes of AuBNPs are shown in Figure S17 (Supporting Information).

The 3.5 wt% CNCs (CNC-2) co-assembled with a series of AuBNPs were compared with AuBNP/CNC-1 chiral composite films to investigate the coupling of the plasmon bands with a stronger chiral photonic background. The higher initial concentration leads to more periods and a red shift of the PBG.[28] The CD and UV–Vis–NIR transmission spectra of the AuBNP/CNC-2 chiral composite films are shown in **Figure 4**a,c and Figure S15 (Supporting Information). Because the plasmonic

CD signals are relatively feebler than background CD signals, the emergence of characteristic CD line shapes was barely observed in strong background chiral responses, as well as in the previous study.[34] We further simulated the CD signals of chiral composite films and separated the extinction of AuBNPs from the background modeled with more periods for stronger chirality (Figure 4d,e). The differences in the extinction wavelengths of AuBNPs for LCP and RCP light were also observed. This means that plasmonic chirality also exists in a stronger photonic background but is difficult to directly observe with CD spectroscopy. However, in the infrared region of B-3/CNC-2, the characteristic CD line shape was observed (Figure 4c), owing to the decrease in background CD signals at the edge of the PBG, which makes it difficult to conceal the plasmonic CD signals. The local electric fields and surface charge distribution profiles of the AuBNPs in the CNCs are shown in Figure 4g,h and Figure 4f, respectively. The asymmetric electric
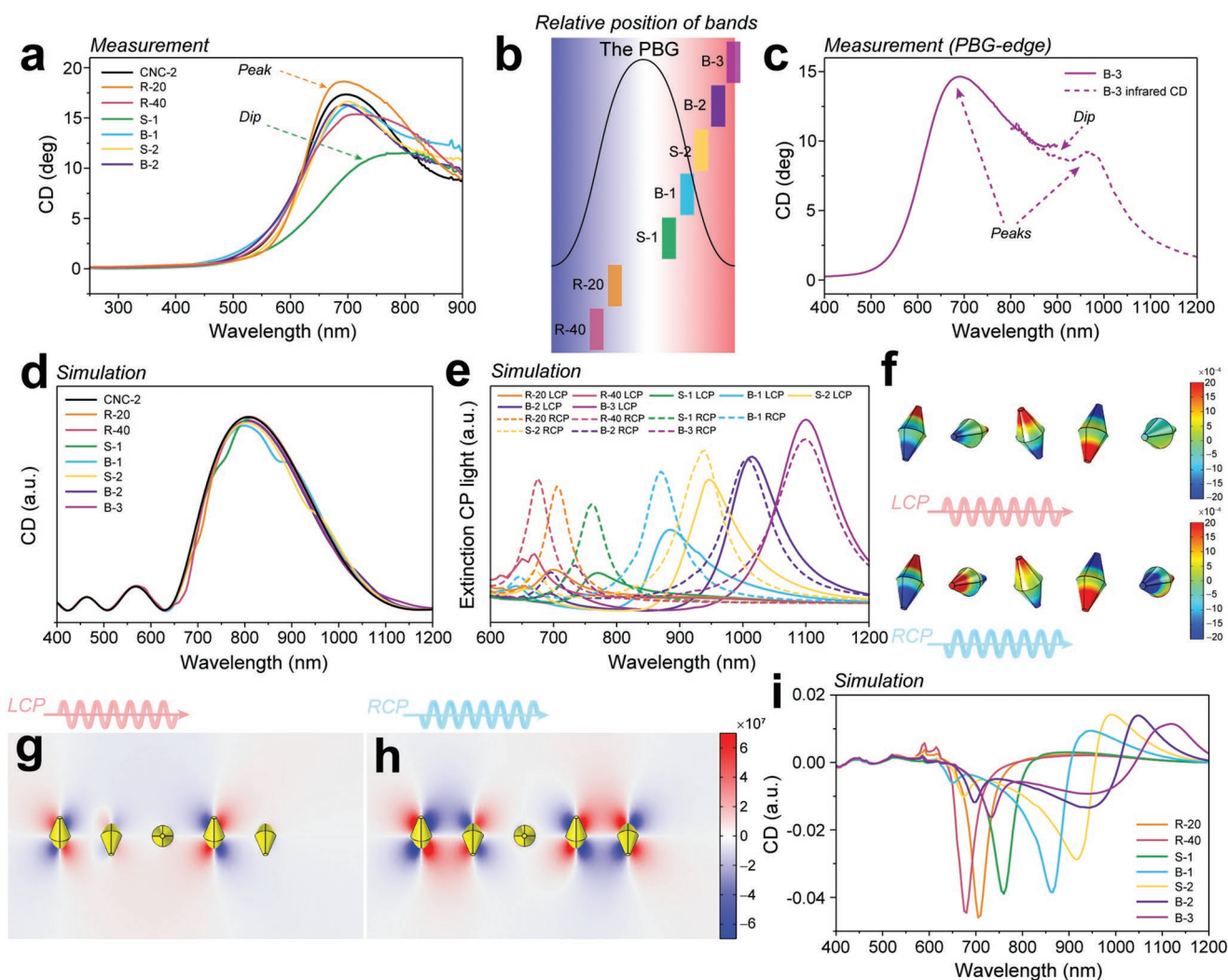
**ADVANCED
SCIENCE NEWS**

www.advancedsciencenews.com

**ADVANCED
FUNCTIONAL
MATERIALS**

www.afm-journal.de

Figure 4. a) Measured CD spectra of AuBNP/CNC-2 composite films and the CNC-2 film. b) Schematic of relative positions between plasmon bands and the PBG of CNC-2. c) Measured CD spectra of B-3/CNC-2 composite films. d) Simulated CD spectra of AuBNP/CNC-2 composite films. e) Simulated extinction spectra for LCP and RCP light of AuBNPs in CNC background f) LCP and RCP light induced surface charge distribution profiles of AuBNPs in CNC background. g) LCP light induced local electric field of AuBNP/CNC. h) RCP light induced local electric field of AuBNP/CNC. i) Simulated independent CD spectra of AuBNPs with plasmonic–photonic coupling states.

field enhancement and oscillation modes of the AuBNPs were similar in chiral photonic backgrounds with different intensities, which indicates that they follow the same mechanism. In addition, the stronger plasmonic–photonic coupling can generate stronger plasmonic chirality of AuBNPs (Figure 4i).

An experiment was designed to verify whether these unique responses would occur when plasmon bands and PBGs were uncoupled. The AuBNPs were assembled with 3.5 wt% CNCs with added extra NaCl (CNC-3), and the measured CD and UV–Vis–NIR transmission spectra are shown in **Figure 5**a and Figure S16 (Supporting Information), respectively. Complete separation of the LSPR bands and PBG was observed in UV–Vis–NIR transmission spectra. As shown in Figure 5a, all CD spectra of the AuBNP/CNC-3 chiral composite films retained the original line shape of CNC CD. We further investigated the independent excitation of AuBNPs for LCP and RCP light. The extinction of RCP light shifted to longer wavelengths

than that of LCP light, and the difference in extinction wavelengths decreased, which induced the characteristic CD line shapes to vanish. This is because the local background fields of each AuBNP are basically identical and achiral outside the PBG. The local electric field distributions (Figure 5f,g) in the uncoupled state show that the LCP light is not moderated by the chiral nematic structure when the system is excited outside the PBG. The independent CD of AuBNPs turned to a peak-dip CD with low intensities from the dip-peak CD signals with coupling states. It is considered that the scattering-induced chirality vanishes under achiral excitation fields outside the PBG. Meanwhile, the dip-peak CD signals were generated by near-field plasmon–plasmon couplings because of the decrease in CNC pitches caused by the smaller distances between AuBNPs.

To numerically analyze the unique chiral responses, we further developed a transfer-matrix method to study complex collective plasmonic scattering by chiral arrangements of AuBNPs
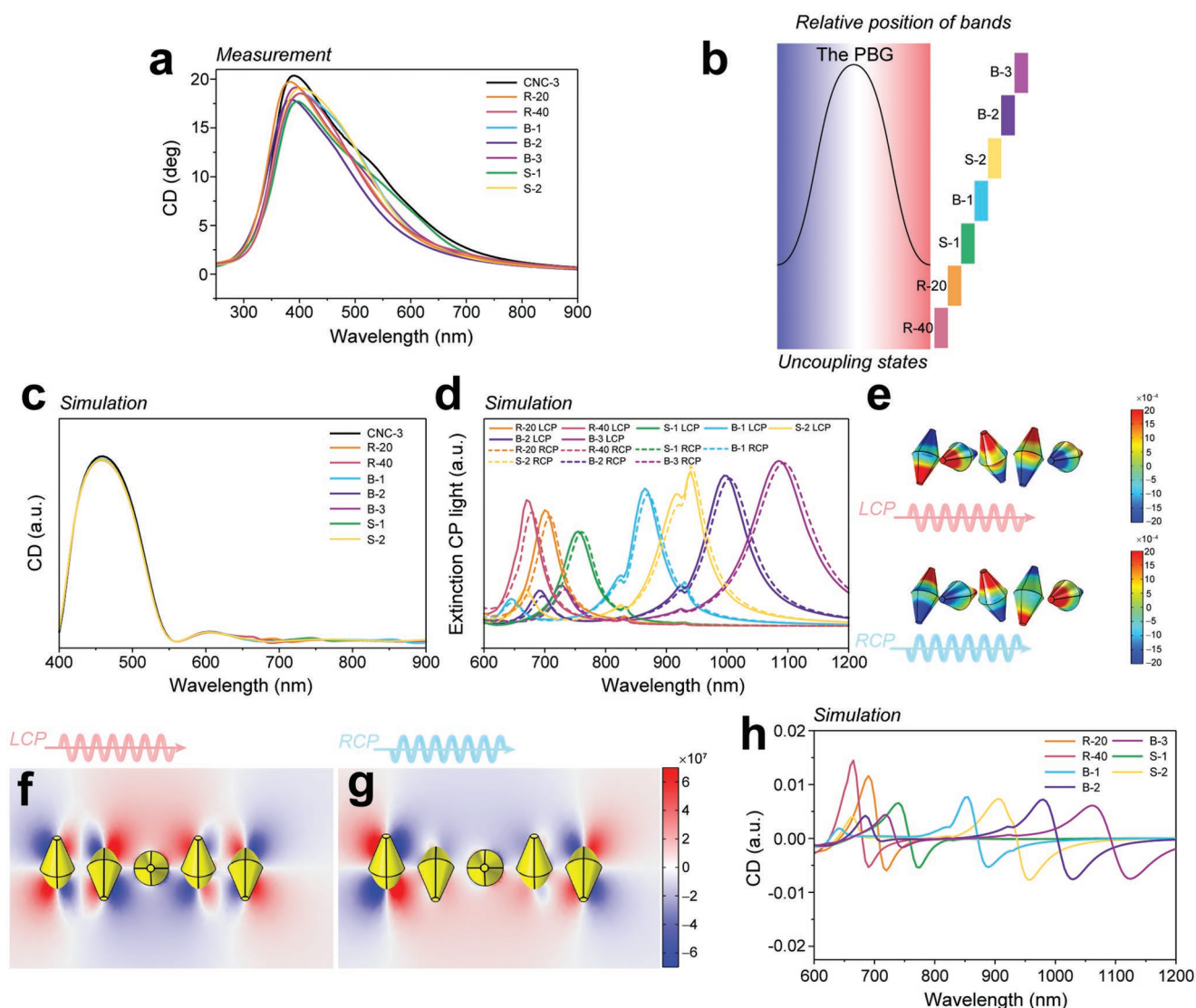
Figure 5. a) Measured CD spectra of AuBNP/CNC-3 composite films and the CNC-3 film. b) Schematic of relative positions between plasmon bands and the PBG of CNC-3. c) Simulated CD spectra of AuBNP/CNC-3 composite films and the CNC-3 film. d) Simulated extinction spectra for LCP and RCP light of AuBNPs in CNC background. e) LCP and RCP light induced surface charge distribution profiles of AuBNPs in CNC background. f) LCP light induced local electric field of AuBNP/CNC. g) RCP light induced local electric field of AuBNP/CNC. h) Simulated independent CD spectra of AuBNPs with uncoupling states.

in the cholesteric structure of CNCs. As shown in **Figure 6**a, we consider the AuBNP/CNC chiral composite films as a pile of rotational anisotropic metal and CNC layers. We first divided the pitch of the chiral composite into N of the metal layers and CNC layers and described the wave propagation inside a single layer. For a single layer of CNC, we use a rotation operation to obtain the permittivity matrix of a single layer.

$$\overset{\leftrightarrow}{\varepsilon}_n = \overrightarrow{Rt}(-\phi_n)\overset{\leftrightarrow}{\varepsilon}\,\overrightarrow{Rt}(\phi_n) \tag{3}$$

Then, eigen electric and eigen magnetic vectors of a single layer can be obtained by substituting the permittivity matrix of a single layer into Maxwell's equations. According to a previous study, the total transfer matrix of the background can be obtained by successively connecting the boundary matrices D and propagation matrices P at each position.[35] We acquired the background transition matrix M under a single pitch to describe the CNC background using the obtained eigen electric and eigen magnetic vectors:

$$M = D_N^{-1}D_{N-1}P_{N-1}D_{N-1}^{-1}D_{N-2}P_{N-2}\ldots D_{n+1}^{-1}D_nP_n\ldots D_1^{-1}D_0P_0 \tag{4}$$

The transition matrix of a background with multiple pitches (such as s pitches) can be obtained simply by taking the M matrix to the sth power.

For a single metal layer, we consider the AuBNPs as uniaxial harmonic oscillators and use temporal coupled-mode theory to obtain the scattering matrices S of uniaxial harmonic oscillators.[36] Next, the S matrices are converted to metal transfer matrices T through an algebraic operation.
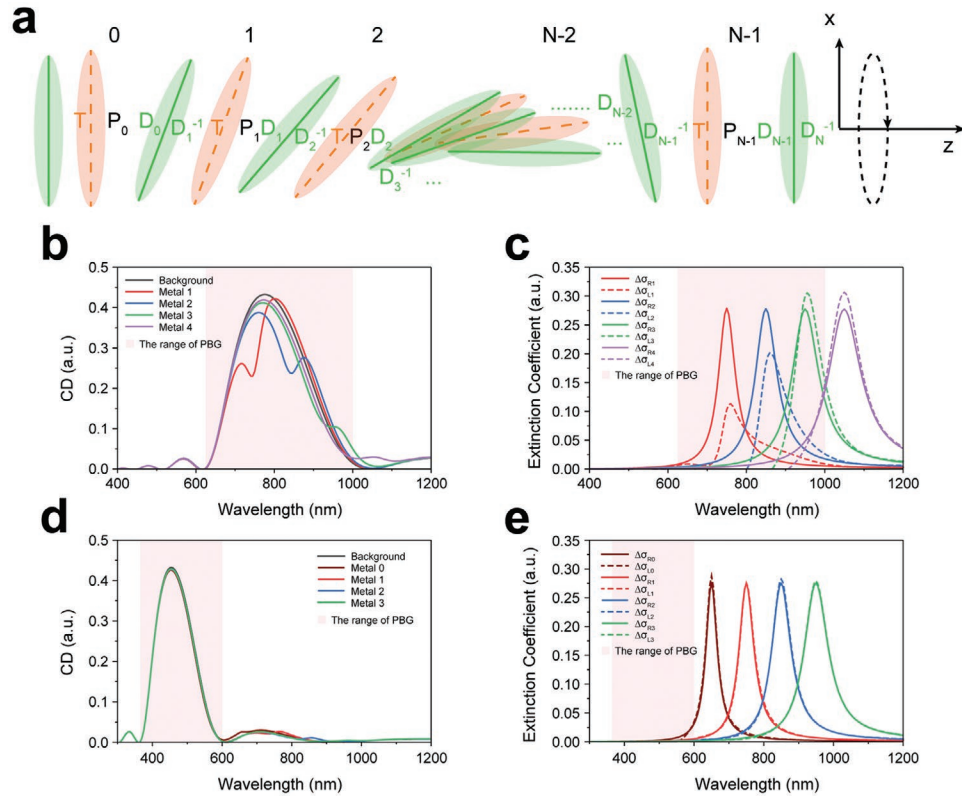
Figure 6. a) Schematic stratification of a left-handed chiral composited structure consisting of N layers of plasmonic materials embedded chiral photonic crystals. b) Calculated CD spectra by using the transfer-matrix method with the PBG (≈615–1000 nm). c) Calculated extinction spectra by using the transfer-matrix method with the PBG (≈615–1000 nm). d) Calculated CD spectra by using the transfer-matrix method with the PBG (≈365–600 nm). e) Calculated extinction spectra by using the transfer-matrix method with the PBG (≈365–600 nm).

The total transfer matrix of the composite system can be considered to be stacked up by N quasi-continuous rotating composite layers. We inserted the metal transfer matrix T into the transfer matrix of each background layer ($D_n^{-1} D_n P_n$), and then the total transfer matrix Q of the composite system of one pitch could be obtained.

$$Q = D_N^{-1} D_{N-1} P_{N-1} T D_{N-1}^{-1} D_{N-2} P_{N-2} T ... D_{n+1}^{-1} D_n P_n T ... D_1^{-1} D_0 P_0 T \qquad (5)$$

Similarly, the transition matrix of the background with s pitches only needs to take the Q matrix to the sth power.

The transmission coefficients of the LCP and RCP (t_{LL} and t_{RR}) under the incidence of circularly polarized light in this system can be easily derived by transforming the total transfer matrix to the circular polarization basis. The extinction coefficients of the incident LCP and RCP light are defined as $\sigma_L = 1 - |t_{LL}|^2$ and $\sigma_R = 1 - |t_{RR}|^2$, respectively. Therefore, the CD of the composite system can be obtained by:

$$CD = \sigma_L - \sigma_R \qquad (6)$$

In addition, the contribution of AuBNPs to the extinction coefficient of the system was calculated by deducting the extinction coefficient of the CNC background from the total extinction coefficient of the system.

$$\Delta \sigma_{L(R)} = \sigma_{L(R)} - \sigma_{L(R)}^{Background} \qquad (7)$$

Using our transfer-matrix method, we calculated the CD spectra and extinction of plasmonic NPs for LCP and RCP light under a chiral excitation field. The results agree well with the experimental observations and the finite element method (FEM) simulation. In Figure 6b, the characteristic CD line shapes and extinction dispersion for LCP and RCP light, generated by the scattering of the chiral arrangement of plasmonic nanoparticles, are observed inside the PBG because the chiral excitation field given by CNCs only exists in the PBG. In contrast, the characteristic CD line shapes and extinction dispersion for the LCP and RCP light vanish when the plasmon bands are outside the PBG. The difference in scattering-induced chirality and the chirality of near-field plasmon-plasmon coupling can be observed in the simulations results (Figure 5e; Figure S20, Supporting Information) and numerical calculations (Figure 6e) outside the PBG. Owing to the small distances between the AuBNPs in CNC-3, weak near-field plasmon-plasmon couplings generate peak-dip CD (Figure 5h), which differ from a dip-peak CD of scattering-induced chirality in the simulation results (Figures 3i and 4i). However, using our transfer-matrix method, only the behavior of plasmonic scattering is considered, effectively eliminating the influence of near-field plasmon–plasmon coupling (Figure 6e). These results prove that the unique chiral responses originating from plasmonic–photonic coupling are generated by multiple plasmonic scatterings by chiral arrangements of AuBNPs under the chiral excitation field provided by the CNCs.

3. Conclusions

In summary, we investigated the effects of plasmonic–photonic couplings on CD responses by combining the quasi-continuous plasmonic resonances with different PBGs of CNC templates. Quasi-continuous plasmon bands were designed by fine-tuning the morphologies of the AuBNPs. The intensity changes of the chiral photonic responses and shifts of the PBGs were achieved by controlling the concentration of CNCs and adding electrolytes. The characteristic dip-peak line shapes, which are highly dependent on the states of plasmonic–photonic couplings, were observed in SP-CD. Furthermore, by separating the responses of AuBNPs from the CNC backgrounds, the dispersions of extinction wavelengths for LCP and RCP light were discovered. This extinction dispersion is considered to be the origin of SP-CD and plasmonic chirality. This plasmonic chirality, determined by the coupling states, is proven to originate from a multiple scattering combination of plasmonic NPs under a chiral excitation field. A novel transfer-matrix method was established to perform numerical analysis of this complex multiple scattering efficiently. This study successfully addresses the problem of how to explain the generation of SP-CD signals and the origin of plasmonic chirality in plasmonic NP/CNC chiral composite films, which establishes a fundamental understanding of plasmonic chirality from chiral templates for further research.

4. Experimental Section

Chemicals and Materials: Benzyldimethylhexadecylammonium chloride (BDAC, 95%), citric acid (CA, ≥99%), and microcrystalline cellulose were purchased from Alfa Aesar. Hexadecyltrimethylammonium chloride (CTAC, ≥98%) was purchased from Sigma–Aldrich. One molar standard hydrochloric acid, $HAuCl_4 \cdot 3H_2O$ (98%), and sulfuric acid (98%) were supplied by Sinopharm Chemical Reagent. L-ascorbic acid (AA, ≥99%), $NaBH_4$ (≥98%), $AgNO_3$ (99.8%), and hexadecyl trimethyl ammonium bromide (CTAB, 99%) were purchased from Aladdin. These abovementioned chemicals and materials were used as received without further purification.

Synthesis of Seed Solution and Gold Bipyramids: The initial gold seeds were synthesized according to the thermal aging method.[37] Five hundred microlitres of 25×10^{-3} M $HAuCl_4$ aqueous solution and 2.5 mL of 100×10^{-3} M CA were added in 48 mL of 500×10^{-3} M CTAC. Then 1.25 mL of 25×10^{-3} M ice-cold $NaBH_4$ was added with vigorous stirring for 5 min. The mixture turned brownish during stirring, signifying the formation of initial gold seeds. Subsequently, the seed solution was aged in an oil bath at 80 °C for 90 min with gentle stirring. Finally, the color of the seed solution changed from brownish to scarlet and was subsequently stored at ≈3 °C to protect from further aging. This aging procedure can markedly improve the yield of gold bipyramids and the product does not require further purification.

According to the previous report, 2 mL of 25×10^{-3} M $HAuCl_4$, 1 mL of 10×10^{-3} M $AgNO_3$, 2 mL of 1 M HCl, 800 μL of 0.1 M AA, and 7 mL of seed solution were mixed into 100 mL of 100×10^{-3} M CTAB aqueous solution.[38] The mixture was then gently stirred at 30 °C for 2 h to allow the gold seeds to grow into bipyramids. The reaction product was centrifuged at 10 000 rpm to remove residual reactants and surfactants. Finally, the bipyramids were redispersed in 15 mL of 1×10^{-3} M CTAB solution to protect the bipyramids from aggregation for subsequent regrowth procedures.

Regrowth of AuBNPs: Gold bipyramid solutions were added to regrowth solutions containing varying amounts of 100×10^{-3} M CTAB, 100×10^{-3} M CTAC, 25×10^{-3} M $HAuCl_4$, 10×10^{-3} M $AgNO_3$, 1 M HCl, and 100×10^{-3} M AA. Details of the amounts of the agents used are shown in Table S1 (Supporting Information). The solution was then incubated at 30 °C for 2 h

under gentle stirring. The reaction product was centrifuged at 10 000 rpm to remove any extra reactant and surfactant. Finally, the obtained AuBNPs were redispersed in 1 mL of 1×10^{-3} M CTAB for further use.

Etching and Regrowth of Etched AuBNPs: Gold bipyramids (1.5 mL) in 1×10^{-3} M CTAB were added to 1.5 mL of 100×10^{-3} M DBAC with gentle stirring. Subsequently, 30 μL of 25×10^{-3} M $HAuCl_4$ was added to the above solution as an oxidative etching agent. The etching procedure was conducted at 30 °C for 20 and 40 min (for R-20 and R-40) under gentle stirring. After the etching procedure, the resulting solution was centrifuged at 10 000 rpm for 5 min to remove residual $HAuCl_4$. The etched AuBNPs were re-dispersed in 1 mL of 1×10^{-3} M CTAB for further use.

The regrowth procedure for the etched AuBNPs was similar to that for the unetched AuBNPs. One millilitre of etched AuBNPs (etched to different extents) were added to 9 mL of 100×10^{-3} M CTAB, 40 μL of 25×10^{-3} M $HAuCl_4$, 20 μL of 10×10^{-3} M $AgNO_3$, 200 μL of 1 M HCl, and 20 μL of 100×10^{-3} M AA. The solution was then incubated at 30 °C for 2 h with gentle stirring. The centrifugation and redispersion procedures were the same as those described above.

Preparation of CNC Suspensions: CNC suspensions were prepared using a typical acid hydrolysis procedure.[22] Twenty grams of microcrystalline cellulose was hydrolyzed with 200 mL of 64 wt% sulfuric acid at 45 °C for 60 min. The reaction was stopped by adding 1 L of ice-cold water. The products were washed with ultrapure water by repeated centrifugation (6000 rpm, 15 min) to remove excess acid until cloudy CNCs were observed in the supernatant. The CNC sediments were then dialyzed in 10 kDa dialysis tubes against ultrapure water for 10 days. Finally, the CNC suspensions were sonicated using a probe ultrasonicator at 600 W for 15 min in an ice bath for homogenization and to increase the helical pitch of the CNCs.

Preparation of AuBNPs/CNC Chiral Composite Films: First, the AuBNPs were washed twice with ultrapure water to eliminate the surfactant effects. Then, ≈6×10^{-7} mol of AuBNPs were added to 4 mL of 1.5 wt % CNC suspensions, 4 mL of 3.5 wt % CNC suspensions, and 4 mL of 3.5 wt % CNC suspensions to which 50 μL of 0.1 M NaCl had been added. The blends were then vigorously mixed using a vortex mixer and bath-sonicated for 1 min to obtain homogenous mixtures. These mixtures were then naturally evaporated in 35-mm diameter polystyrene Petri dishes at ambient conditions (30 °C, 80% RH) for 5 days to form AuBNPs/CNC composite films. Simultaneously, identical CNC suspensions without AuBNPs were evaporated to form films for comparison purposes.

Characterization: The UV–Vis–NIR absorption spectra of the AuBNP dispersions from 300 to 1300 nm and the transmission spectra of a series of freestanding films from 250 to 1300 nm were measured using a PerkinElmer Lambda 950 UV–Vis–NIR spectrophotometer equipped with a 150 mm integrating sphere. TEM images of the AuBNPs and CNCs were obtained using an FEI Talos L120C G2 operating at an acceleration voltage of 120 kV. SEM images were obtained using a TESCAN RISE operating in the 1 kV secondary electron mode. CD spectra were recorded using a Jasco J-1500 circular dichroism spectrometer in transmission mode. The films were mounted normal to the circularly polarized incident beam and the spectra in the wavelength range of 250–900 nm were measured using a Xe lamp source and a PMT detector. The near-infrared CD spectra from 800 to 1200 nm were measured using a tungsten lamp and an InGaAs detector. Polarized optical microscopy (POM) images were obtained using a Zeiss Primotech Pol microscope. The zeta potential and DLS test of the 0.01 wt% diluted CNC suspension were measured using a Brookhaven omni zeta potential difunctional characterization at 25 °C.

Finite Element Method (FEM) Simulations: The simulation results of the FEM include the CD spectra, extinction spectra, local electric field distribution, and surface charge distribution profiles were obtained using the commercial software package COMSOL Multiphysics. The sizes of the AuBNPs were based on TEM images and the morphologies of the AuBNPs were simplified to bicones. The CNC background was created using a dielectric constant matrix that can efficiently describe the optical properties of the left-handed helical CNCs. The expression for this dielectric constant matrix is shown in Supporting Information. The

pitches of the CNC background used in the modeling were measured using cross-sectional SEM images. This system was illuminated by LCP and RCP light with an incident parallel to the helical axis of the AuBNPs and the CNC background. Two analysis ports were set in the front and back of the system to record the reflected and transmitted light. The simulation model is shown in Figure S18 (Supporting Information). The number of periodicities (*n*) for simulating AuBNP/CNC-1 is 1. The *n* for simulating AuBNP/CNC-2 and AuBNP/CNC-3 is 1.5. The length of cell boundary (*a*) is 1200 nm. The boundaries of AuBNP/CNC cells were defined as periodic boundaries. The top and bottom boundaries of the calculation region were defined with a perfectly matched layer (PML). The orientation of the helical AuBNPs and CNC background was set to be consistent, according to the previous study.[29] The local electric field distribution and surface charge distribution profiles were produced with S-1/CNC background excited by the 770 nm LCP and RCP light.

Transfer-Matrix Method Calculation: The CD and extinction spectra calculated using the transfer-matrix method were obtained using Mathematica. The computational methodology of the transfer-matrix method is discussed in more detail in Supporting Information.

Supporting Information

Supporting Information is available from the Wiley Online Library or from the author.

Conflict of Interest

The authors declare no conflict of interest.

Data Availability Statement

Research data are not shared.

[1] V. Davankov, *Chirality* **2006**, *18*, 459.
[2] A. Rodger, B. Nordén, *Circular Dichroism: Principles and Applications*, Oxford University Press, New York, USA **1997**.
[3] Z. Hu, D. Meng, F. Lin, X. Zhu, Z. Fang, X. Wu, *Adv. Opt. Mater.* **2019**, *7*, 1801590.
[4] X. Duan, S. Kamin, F. Sterl, H. Giessen, N. Liu, *Nano Lett.* **2016**, *16*, 1462.
[5] N. J. Greybush, V. Pacheco-Peña, N. Engheta, C. B. Murray, C. R. Kagan, *ACS Nano* **2019**, *13*, 3875.
[6] M. Hentschel, M. Schäferling, X. Duan, H. Giessen, N. Liu, *Sci. Adv.* **2017**, *3*, e1602735.
[7] A. O. Govorov, *J. Phys. Chem. C* **2011**, *115*, 7914.
[8] X. Lan, Q. Wang, *Adv. Mater.* **2016**, *28*, 10499.
[9] Z. Cao, H. Gao, M. Qiu, W. Jin, S. Deng, K. Wong, D. Lei, *Adv. Mater.* **2020**, *32*, 1907151.
[10] E. S. A. Goerlitzer, A. S. Puri, J. J. Moses, L. V. Poulikakos, N. Vogel, *Adv. Opt. Mater.* **2021**, *9*, 2100378.
[11] V. K. Valev, J. J. Baumberg, C. Sibilia, T. Verbiest, *Adv. Mater.* **2013**, *25*, 2517.
[12] M. Qiu, L. Zhang, Z. Tang, W. Jin, C. Qiu, D. Y. Lei, *Adv. Funct. Mater.* **2018**, *28*, 1803147.
[13] Z. Y. Bao, J. Dai, Q. Zhang, K. H. Ho, S. Li, C. H. Chan, W. Zhang, D. Y. Lei, *Nanoscale* **2018**, *10*, 19684.
[14] R. Tullius, A. S. Karimullah, M. Rodier, B. Fitzpatrick, N. Gadegaard, L. D. Barron, V. M. Rotello, G. Cooke, A. Lapthorn, M. Kadodwala, *J. Am. Chem. Soc.* **2015**, *137*, 8380.
[15] J. R. Mejía-Salazar, O. N. Oliveira, *Chem. Rev.* **2018**, *118*, 10617.
[16] J. Zhou, J. Dong, B. Wang, T. Koschny, M. Kafesaki, C. M. Soukoulis, *Phys. Rev. B* **2009**, *79*, 121104.
[17] W. Li, Z. J. Coppens, L. V. Besteiro, W. Wang, A. O. Govorov, J. Valentine, *Nat. Commun.* **2015**, *6*, 8379.
[18] L. Gui, M. Hentschel, J. Defrance, J. Krauth, T. Weiss, H. Giessen, *ACS Photonics.* **2019**, *6*, 3306.
[19] J. Mosquera, Y. Zhao, H. J. Jang, N. Xie, C. Xu, N. A. Kotov, L. M. Liz-Marzán, *Adv. Funct. Mater.* **2020**, *30*, 1902082.
[20] A. Kuzyk, R. Schreiber, Z. Fan, G. Pardatscher, E. M. Roller, A. Högele, F. C. Simmel, A. O. Govorov, T. Liedl, *Nature* **2012**, *483*, 311.
[21] J. Lu, Y. Xue, K. Bernardino, N. N. Zhang, W. R. Gomes, N. S. Ramesar, S. Liu, Z. Hu, T. Sun, A. F. de Moura, N. A. Kotov, K. Liu, *Science* **2021**, *371*, 1368.
[22] D. Bondeson, A. Mathew, K. Oksman, *Cellulose.* **2006**, *13*, 171.
[23] B. Frka-Petesic, G. Guidetti, G. Kamita, S. Vignolini, *Adv. Mater.* **2017**, *29*, 1701469.
[24] Y. Habibi, L. A. Lucia, O. J. Rojas, *Chem. Rev.* **2010**, *110*, 3479.
[25] R. J. Moon, A. Martini, J. Nairn, J. Simonsen, J. Youngblood, *Chem. Soc. Rev.* **2011**, *40*, 3941.
[26] B. Frka-Petesic, H. Radavidson, B. Jean, L. Heux, *Adv. Mater.* **2017**, *29*, 1606208.
[27] A. Tran, W. Y. Hamad, M. J. MacLachlan, *Langmuir* **2018**, *34*, 646.
[28] R. M. Parker, G. Guidetti, C. A. Williams, T. Zhao, A. Narkevicius, S. Vignolini, B. Frka-Petesic, *Adv. Mater.* **2018**, *30*, 1704477.
[29] Q. Liu, M. G. Campbell, J. S. Evans, I. I. Smalyukh, *Adv. Mater.* **2014**, *26*, 7178.
[30] C. Duan, Z. Cheng, B. Wang, J. Zeng, J. Xu, J. Li, W. Gao, K. Chen, *Small* **2021**, *17*, 2007306.
[31] A. Querejeta-Fernández, G. Chauve, M. Methot, J. Bouchard, E. Kumacheva, *J. Am. Chem. Soc.* **2014**, *136*, 4788.
[32] A. Lukach, H. Thérien-Aubin, A. Querejeta-Fernández, N. Pitch, G. Chauve, M. Méthot, J. Bouchard, E. Kumacheva, *Langmuir* **2015**, *31*, 5033.
[33] G. Chu, X. Wang, H. Yin, Y. Shi, H. Jiang, T. Chen, J. Gao, D. Qu, Y. Xu, D. Ding, *ACS Appl. Mater. Interfaces* **2015**, *7*, 21797.
[34] Z. Cheng, Y. Ma, L. Yang, F. Cheng, Z. Huang, A. Natan, H. Li, Y. Chen, D. Cao, Z. Huang, Y. H. Wang, Y. Liu, R. Yang, H. Zhu, *Adv. Opt. Mater.* **2019**, *7*, 1801816.
[35] J. Hao, L. Zhou, *Phys. Rev. B* **2008**, *77*, 094201.
[36] S. Fan, W. Suh, *J. Opt. Soc. Am. A* **2003**, *20*, 569.
[37] A. Sánchez-Iglesias, N. Winckelmans, T. Altantzis, S. Bals, M. Grzelczak, L. M. Liz-Marzán, *J. Am. Chem. Soc.* **2017**, *139*, 107.
[38] J. H. Lee, K. J. Gibson, G. Chen, Y. Weizmann, *Nat. Commun.* **2015**, *6*, 7571.